Automatic optical inspection system for 3D surface profile measurement of multi-microlenses using the optimal inspection path

View the table of contents for this issue, or go to the journal homepage for more

Automatic optical inspection system for 3D surface profile measurement of multi-microlenses using the optimal inspection path

Shih-Wei Yang and Shir-Kuan Lin

Institute of Electrical and Control Engineering, National Chiao Tung University, Hsinchu, Taiwan

E-mail: swyang.nctu@msa.hinet.net

Abstract

In this paper, an automatic optical inspection system is proposed for measuring the three-dimensional surface profile of multi-microlenses according to the optimal inspection path. The proposed system is applicable for full and sampling inspection of microlens arrays, and has the following contributions: (1) the optimal inspection path of sampling inspection is derived by a Genetic Algorithm considering the acceleration characteristic of the XY-table. (2) The incomplete microlens fringe is removed, and the center of each microlens can be automatically positioned. (3) The phase difference of each neighboring pixel is calculated through the concept of sign reversal in order to rebuild the surface profile. According to the experimental results, the lens sag of microlenses in different sizes can be correctly measured by the proposed system, and a relative error of 3.4% (max) can be achieved. Compared with other methods, the positioning time of the proposed method is shortened by 10% to 30%, validating the practicability of this system.

Keywords: automatic optical inspection system, multi-microlenses, three-dimensional surface profile, optimal inspection path

(Some figures may appear in colour only in the online journal)

1. Introduction

The microlens array has been extensively used in the field of consumer electronics, and the permissible specification error is very small. Therefore, many methods for measuring the microlens surface profile have been proposed, which can be mainly divided into contact and non-contact measurements. The former includes the scanning electron microscope, atomic force microscope [1–5], etc. This type of instrument provides good accuracy; however, the scanning process is usually time consuming, and the contact probe is likely to scratch the surface of the microlens. Thus, it is not suitable for the in-line inspection of industrial application.

In the non-contact measurement of the surface profile, the phase shifting interferometry [6–11] requires multiple fringe patterns to reconstruct the surface profile of an object.

Although the measurement accuracy is high, it is also computationally expensive. The Fourier transform method [12–15] only needs a single image to determine the phase of the interference fringe. However, it is inapplicable to the closed fringes. In addition, a complex experimental setup is required for introducing the special carrier, which increases the cost. In the former researches [16, 17], we measured the two-dimensional (2D) and three-dimensional (3D) surface profile of a single microlens by the principle of Fizeau interferometer. The absolute value of the phase difference is directly used to calculate the lens sag, without considering the sign reversal. When the surface profile does not continuously increase or decrease, there may be minor errors in the measurement result. Yang *et al* [18] proposed a directional computing window for searching the skeletons in an ESPI image in order to determine the fringe phases. Lin *et al* [19] used the

grating projection method to rebuild the surface profile of a small lens. However, the above methods lack the function of multi-microlenses positioning, and is only applicable to measure a single microlens. Hence, the proposed system is designed specifically for measuring the 3D surface profile of multi-microlenses in a microlens array based on the Fizeau interferometry, which is easily installed and low cost, in order to improve the above drawbacks.

Since there are numerous lenses in a microlens array, sometimes the manufacturers would only select some representative microlenses for sampling inspection. In such a case, there may not be inspected lenses in the line-scan inspection path for full inspection, thus wasting inspection time. In the former research [20], the XY-table moves according to the inspection path of the minimum total length during sampling inspection. While the inspection path of the minimum total length may not be the optimal path, the minimum path length does not guarantee the shortest time of XY-table positioning.

Based on the above reasons, this paper proposes an automatic optical inspection system for 3D surface profile measurement of multi-microlenses using the optimal inspection path. For full inspection, multi-microlenses are measured simultaneously according to the line-scan inspection path; while for sampling inspection, each selected microlens is measured according to the optimal inspection path, which is planned by a Genetic Algorithm (GA) [20–23] and by considering the acceleration characteristic of the XY-table, in order to increase the efficiency of the sampling inspection. Furthermore, a method for searching the centers of multi-microlenses is also proposed, where the incomplete microlens fringes in the image can be removed, and the complete microlenses can be positioned. The fringe phase is retrieved based on the fringe extreme points, and the 3D surface profiles of multi-microlenses are rebuilt according to the phase difference of neighboring pixels through a single fringe pattern.

2. Inspection path optimization of sampling inspection using Genetic Algorithm

In this study, the fitness function is designed by considering the acceleration characteristics of the XY-table, in order to obtain the optimal inspection path. The design principles are as illustrated in the following sections.

2.1. Definition of the inspection path

In the proposed algorithm, a pseudo coordinate is assigned to each microlens of the microlens array. These pseudo coordinates are ranged from $(1, 1)$ to (n, n), where n is the number of microlenses in a single row. The XY-table moves to the selected microlens for sampling inspection according to these pseudo coordinates. All inspected microlenses form various inspection paths (or called chromosomes) of different inspection orders, and the initial chromosomes are randomly generated. A complete inspection path consists of many subpaths. For every subpath, the displacement in the X and Y

directions is controlled by two stepping motors, respectively. The longer one is defined as the major axis, while the shorter one is defined as the minor axis. The actual length of the major and minor axes is the product of the difference of the pseudo coordinates and lens spacing, as shown in figure 1(a).

2.2. Judgment of the stepping motor reverse

In XY-table positioning, if the current traveling direction of any one of the major or minor axes is opposite to the traveling direction of the next subpath, the corresponding stepping motor should stop before it reverses, as shown in figure 1(b)–(d). This phenomenon would have a severe impact on calculating the positioning time of the XY-table; therefore, a straightforward method is proposed to judge if the stepping motor reverses. According to figure 1(b), the inner product of two vectors (**i** and **j**) corresponding to the consecutive subpaths is positive when both of the stepping motors rotating in the X and Y directions do not need to reverse, which can be written as:

$$\mathbf{i} \cdot \mathbf{j} > 0 \tag{1}$$

where $\mathbf{i} = (x_2 - x_1, y_2 - y_1)$; $\mathbf{j} = (x_3 - x_2, y_3 - y_2)$; (x_1, y_1), (x_2, y_1) and (x_3, y_3) are the pseudo coordinates of the selected microlenses.

If equation (1) is not satisfied, it implies that the XY-table has uniaxial reverse or biaxial reverse in the next subpath; hence, the positioning time of the current subpath should add the suspension time t_{rev} of the stepping motor, where $t_{rev} = 0.5(s)$ in this paper.

2.3. Fitness function of scoring the inspection path

The positioning time of each subpath is the time consumption of finishing traveling the major axis in each subpath, and the summation of the positioning time of all the subpaths is the total positioning time of the XY-table. The total positioning time of the XY-table is used as the fitness of GA for scoring the inspection path in this paper, and we adopt the trapezoidal motion schemes as the model for acceleration and deceleration of the XY-table. Hence, the positioning time of any subpath can be calculated as below:

According to figure 2, the number of total pulses $A_{(i)}$ corresponding to the major axis of any subpath is given by:

$$A_{(i)} = \frac{L_{(i)}}{l_r} \times \frac{360°}{\theta_s} \tag{2}$$

where $L_{(i)}$ is the major axis length of the ith subpath; l_r is the distance moved with one revolution of the stepping motor; θ_s is the step angle.

Let the initial speed of the stepping motor be V_s, and the positioning time of the subpath be $t_{(i)}$. As the acceleration time $t_{a(i)}$ (equal to deceleration time $t_{d(i)}$) and the positioning time $t_{(i)}$ are proportional, let $t_{a(i)} = t_{d(i)} = k \times t_{(i)}$, where k is a proportional constant. According to the allowable maximum acceleration slope m of the adopted XY-table, the maximum speed V_H of the accelerated XY-table can be derived as:

$$V_H = V_s + m \times t_{a(i)}. \tag{3}$$
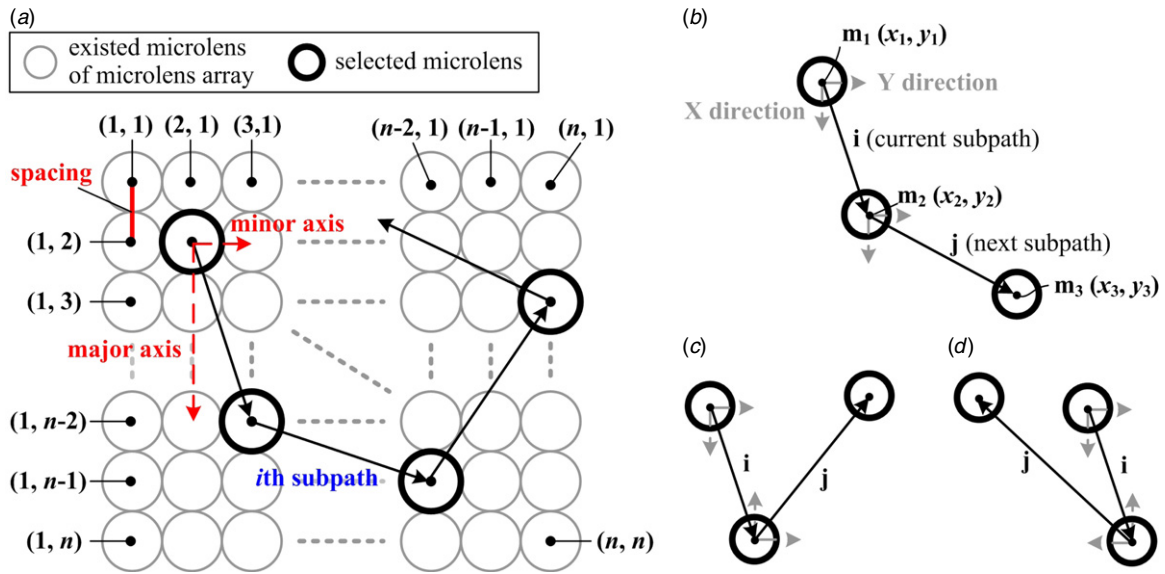
Figure 1. (*a*) Inspection path of the microlens array sampling inspection. (*b*) Definition of the vectors **i**, **j** corresponding to the consecutive subpaths and an example of no motor reverse on both axes. (*c*) An example of uniaxial reverse. (*d*) An example of biaxial reverse.
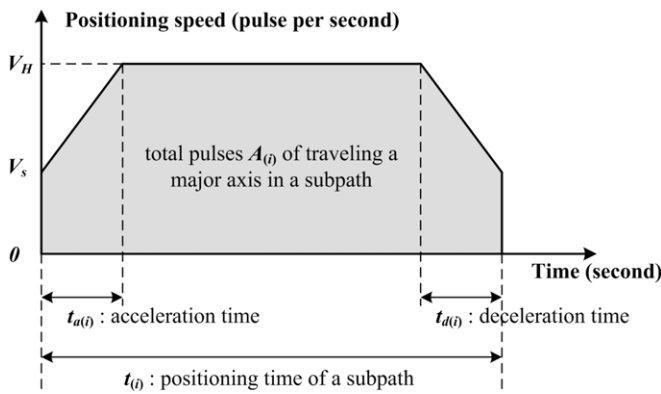
Figure 2. The used trapezoidal motion scheme for XY-table positioning.

The trapezoid area in figure 2 is calculated and $t_{(i)}$ is solved as:

$$t_{(i)} = \frac{-V_s \pm \left(V_s^2 + 4mk(1-k)A_{(i)}\right)^{1/2}}{2mk(1-k)} \qquad (4)$$

where $V_s, A_{(i)}, m$ and $1-k$ are greater than 0, thus, the negative root in equation (4) is unreasonable. Equation (2) is substituted in the positive root of equation (4), and the positioning time $t_{(i)}$ of the subpath can be written as:

$$t_{(i)} = \frac{-V_s + \left(V_s^2 + 4mk(1-k) \times \frac{L_{(i)}}{l_r} \times \frac{360°}{\theta_s}\right)^{1/2}}{2mk(1-k)}. \qquad (5)$$

The XY-table must be accelerated in allowable conditions, more specifically, the number of resulted acceleration pulses must be greater than the limit of the minimum acceleration pulses T_a. This condition can be expressed as:

$$\left(V_s + \frac{mk}{2}\right)kt_{(i)} \geqslant T_a. \qquad (6)$$

If equation (6) is not satisfied, the XY-table moves at a steady speed of V_s, then $t_{(i)}$ should be modified as $A_{(i)}/V_s$. The total positioning time t_{sum} of the XY-table can be obtained from the following equation:

$$t_{sum} = \sum_{i=1}^{N} t_{(i)} + p \times t_{rev} \qquad (7)$$

where N is the number of subpaths; p is the reverse number of the stepping motor.

Note that equation (7) is also the fitness function of GA in the proposed system.

2.4. Crossover and mutation operation

The fitness of each complete inspection path can be determined by equation (7). The paths with higher fitness are selected as the parental chromosomes, and other new inspection paths are generated through these parental chromosomes using crossover and mutation operations, in order to find the optimal inspection path. The crossover method used in this paper is the partially-mapped crossover operation (see [20, 21] for details). The inspection order of microlenses is changed according to a preset probability r_c, and a corresponding example of an inspection path which contains seven microlenses is given in figure 3(*a*). The result of the crossover mutates according to the inversion mutation operation [20] by a probability r_m, to avoid the convergence result falling into the local optimum, as shown in figure 3(*b*).

If the obtained fitness is unchanged after 2000 iterations, the optimal inspection path is converged and found. The XY-table will position according to this optimal result during sampling inspection, and acquires the fringe patterns of selected microlenses one by one.
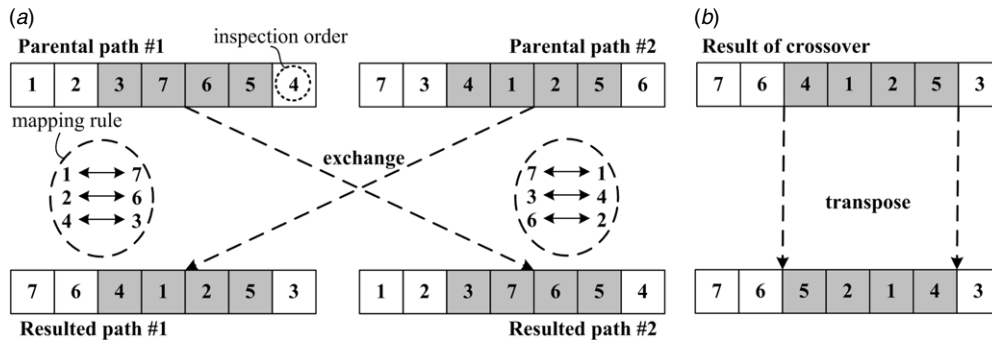
Figure 3. (*a*) Example of partially-mapped crossover operation by an inspection path which contains seven microlenses. (*b*) Result of inversion mutation operation for (*a*).
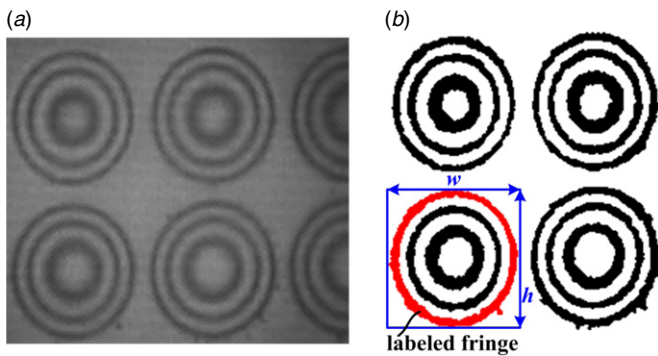
Figure 4. (*a*) Interference fringes of multi-microlenses. (*b*) Result of local thresholding and incomplete fringe removal for (*a*).

3. 3D surface profile measurement of multi-microlenses

3.1. Local thresholding and incomplete fringe removal

The interference fringes of multi-microlenses can be obtained through optical interferometry, as shown in figure 4(*a*). The microscope objective and laser source result in a nonuniform optical field in the image. If the conventional thresholding techniques are used, the microlens and background can sometimes not be correctly separated. Therefore, a mask operation based on the local average values and contrast is used to solve the nonuniformity of the optical field. Let γ be the contrast of the mask, and T_{con} be a preset threshold. If $\gamma \geqslant T_{con}$, the fringe image can be binarized according to the following equation:

$$g^*(x, y) = \begin{cases} 255, & g(x, y) \geqslant M_{avg} \\ 0, & g(x, y) < M_{avg} \end{cases} \qquad (8)$$

where γ is the difference between the maximum gray value and the minimum gray value in the mask; $T_{con} = 20$ in this paper; $g(x, y)$ is the gray value of pixel (x, y) in the mask; $g^*(x, y)$ is the gray value after mask operation; M_{avg} is the average gray value of all pixels in the mask.

While, if $\gamma < T_{con}$, equation (8) must be corrected to:

$$g^*(x, y) = \begin{cases} 255, & M_{avg} \geqslant G_{avg} \\ 0, & M_{avg} < G_{avg} \end{cases} \qquad (9)$$

where G_{avg} is the average gray value of all pixels in the fringe pattern.

However, figure 4(*a*) contains complete and incomplete microlens interference fringes, the incomplete fringes must be removed from the result of thresholding. Each complete and incomplete fringe can be labeled by the connected-component rule, and the complete microlens interference fringe approximates a concentric circle. Therefore, for every labeled fringe, if the aspect ratio of the external quadrangle, i.e. w/h, is very close to 1 (figure 4(*b*)), meaning this labeled fringe is complete and should be reserved; otherwise, the fringe missing the aforesaid condition will be removed, as shown in figure 4(*b*).

3.2. Automatic center positioning of multi-microlenses

In order to automatically locate the center of each microlens in the fringe pattern, the concept of clustering is used for searching the central fringe of each microlens. The diameters of fringes in figure 4(*b*) can be approximated as $(w + h)/2$, these diameters are sorted in ascending order (figure 5(*a*)), and the difference between two consecutive diameters is calculated (figure 5(*b*)).

Set the average μ of diameter differences in figure 5(*b*) as an initial clustering threshold, and these differences are divided by μ into two clusters: the differences less than μ are the first cluster, and the corresponding average μ_1 can be determined; the differences greater than or equal to μ are the second cluster, and the corresponding average μ_2 can also be determined. A new clustering threshold $\mu^* = (\mu_1 + \mu_2)/2$ is obtained. If $\mu = \mu^*$, the clustering process ends; otherwise substitute μ^* for μ and repeat the aforesaid procedure till μ converges. Finally, the resulted μ is the threshold of fringe clustering, as shown in figure 5(*b*). If the difference between two consecutive diameters is greater than μ, the fringes can be divided into two clusters, and the remaining are deduced by the same process. In the result of clustering, the first cluster is the set of central fringes of various microlenses, as shown in figure 5(*c*).

The brightest (or the darkest) point in each central fringe is the microlens center. The distance between these centers is calculated in order to obtain the correct positions of microlenses, as shown in figure 6.
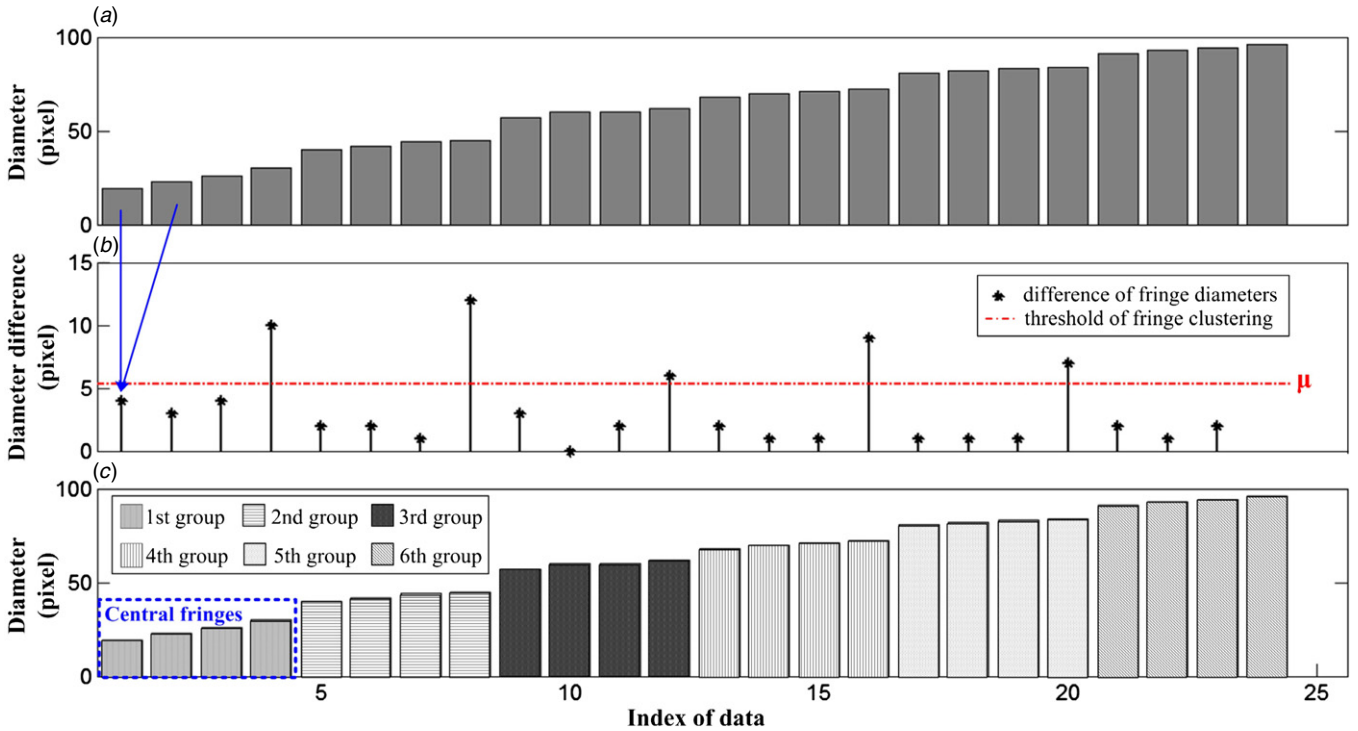
Figure 5. (*a*) Sequence of the fringe diameters. (*b*) Differences of the consecutive fringe diameters. (*c*) Result of fringe clustering.
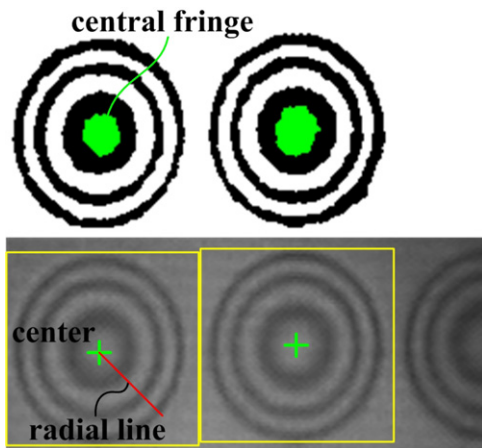

Figure 6. The top image is the obtained central fringes; the bottom image is the corresponding result of fringe center positioning.

3.3. Surface profile reconstruction using the fringe extreme points

The outermost edge point of each microlens can be obtained from figure 4(*b*). The edge points are connected to the microlens center, and each line connection forms a radial line [17]. Along any radial line (figure 6), the corresponding brightness curve of the fringe can be plotted, and the extreme points, i.e. the peaks and valleys, of the brightness curve can be located through comparing the magnitude of the gray value of every pixel on the radial line, as shown in figure 7(*a*). Note that the phase variation in the outermost fringe of the microlens is possibly not a complete 180°, thus, the edge point will not be regarded as an extreme point in the proposed algorithm.

From figure 7(*a*), the gray value of each pixel on the radial line can be normalized as [16, 17]:

$$g_n(i) = 2\frac{g(i) - \Delta(i)}{g_{\text{peak}}(i) - g_{\text{valley}}(i)} \quad (10)$$

where $g(i)$ is the gray value of the ith pixel on the radial line; $g_n(i)$ is the result of normalization; $g_{\text{peak}}(i)$ is the gray value of the peak closest to the ith pixel; $g_{\text{valley}}(i)$ is the gray value of the valley closest to the ith pixel; $\Delta(i) = g_{\text{valley}}(i) + (g_{\text{peak}}(i) - g_{\text{valley}}(i))/2$.

Since the brightness of the fringe is distributed in a cosine curve, according to the interference equation, the phase value of every pixel on the radial line can be calculated through the arccosine function, and the phase difference of every neighboring pixel from the microlens edge to the center along the radial line can be obtained by:

$$\phi(i) = [\cos^{-1}(g_n(i)) - \cos^{-1}(g_n(i-1))] \times (-1)^\alpha \quad (11)$$

where $\phi(i)$ is the phase difference between the ith and the $(i-1)$th pixel on the radial line; α is 0 at the segment from the peak to the valley of the radial line, while α is 1 at the segment from the valley to the peak of the radial line.

The phase distribution and the corresponding phase differences of figure 7(*a*), are shown as figure 7(*b*).

Different from the method in [16, 17], the phase difference of every neighboring pixel is calculated using equation (11) with a sign reversal. The surface height of a specific pixel on the radial line can be obtained by summing up the phase differences from the microlens edge to the target pixel, without using a phase unwrapping method:

$$H(i) = \frac{\lambda}{4\pi} \times \sum_{j=1}^{i} \phi(j) \quad (12)$$
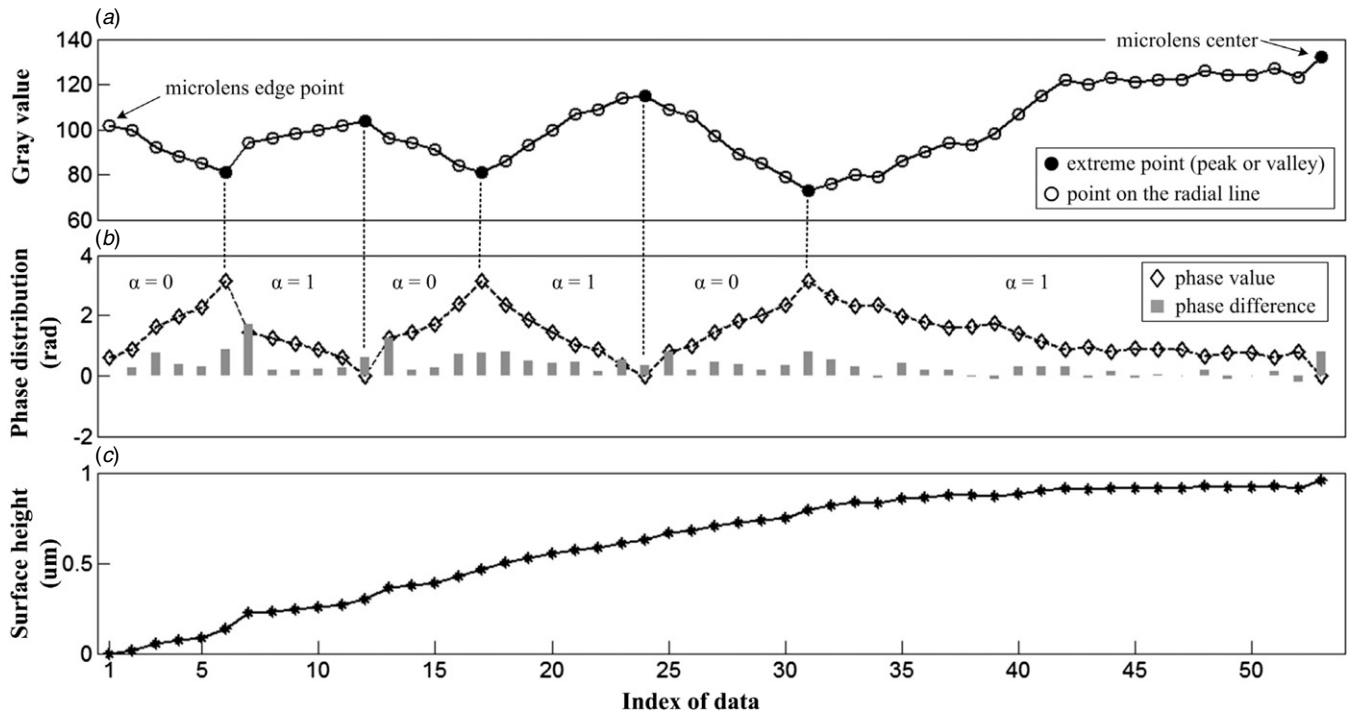
Figure 7. (*a*) Brightness curve of a radial line. (*b*) Phase value of every pixel in (*a*) and the corresponding phase difference. (*c*) Surface height of the radial line in (*a*).

where $H(i)$ is the surface height of the ith pixel on the radial line; λ is the wavelength of the adopted light source.

The surface height of the radial line in figure 7(*a*) is shown in figure 7(*c*), and a complete surface profile of the microlens can be rebuilt through all the radial lines on the microlens fringe pattern.

4. Experimental results and discussion

### 4.1. Experimental setup of the proposed system

The proposed inspection system of multi-microlenses is designed based on the concept of the Fizeau interferometer, and the experimental setup is shown in figure 8. The microlens array sample is placed on the XY-table with a mounting plate, and a laser diode of 680 nm wavelength is used as the system light source. The laser light is transmitted through the fiber bundle to the beam splitter, which then enters the optical flat (reference plane) and the surface of the inspected microlens to form the interference fringe. The arising laser speckle will cause the fringe pattern to become blurred and is removed by a rotating diffuser. The resulting fringe pattern is magnified through a 20× microscope objective, a 1× adapter, and a manual zoom lens, and is captured by a monochrome CCD camera for 3D profile reconstruction.

In full inspection, the XY-table moves according to the line-scan inspection path, and the 3D surface profiles of multi-microlenses are measured simultaneously by a single fringe pattern. While in sampling inspection, the selected microlenses are measured one by one according to the optimal inspection path. The positioning precision of the adopted XY-table is 0.625 μm per pulse, and the self-starting speed is 500 pps. It
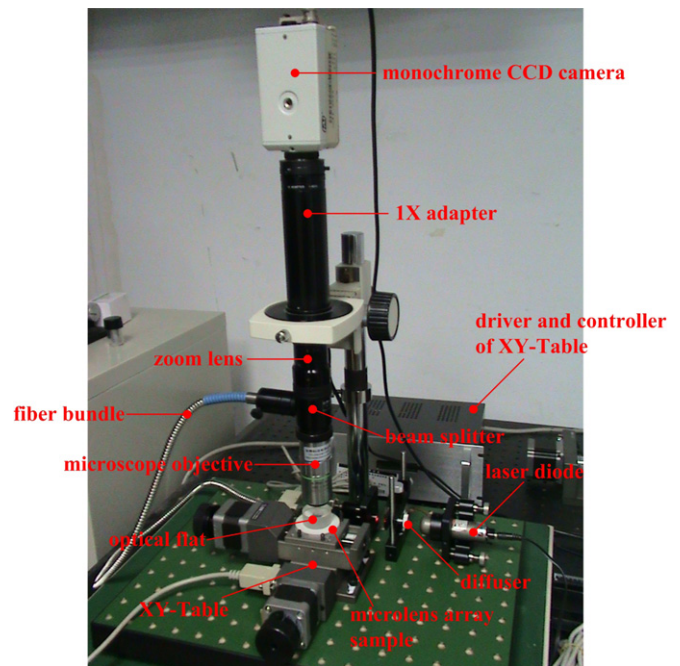
Figure 8. Experimental setup of the proposed system.

should be noted that if the shutter speed of the CCD camera is too low, the XY-table would need to stop at every inspected region for image capture, hence, the time t_{rev} of the motor reverse should be replaced by the stop time of the XY-table at each inspected region. On the contrary, the XY-table would just pass over the inspected microlenses, and t_{rev} in section 2.2 should be considered.
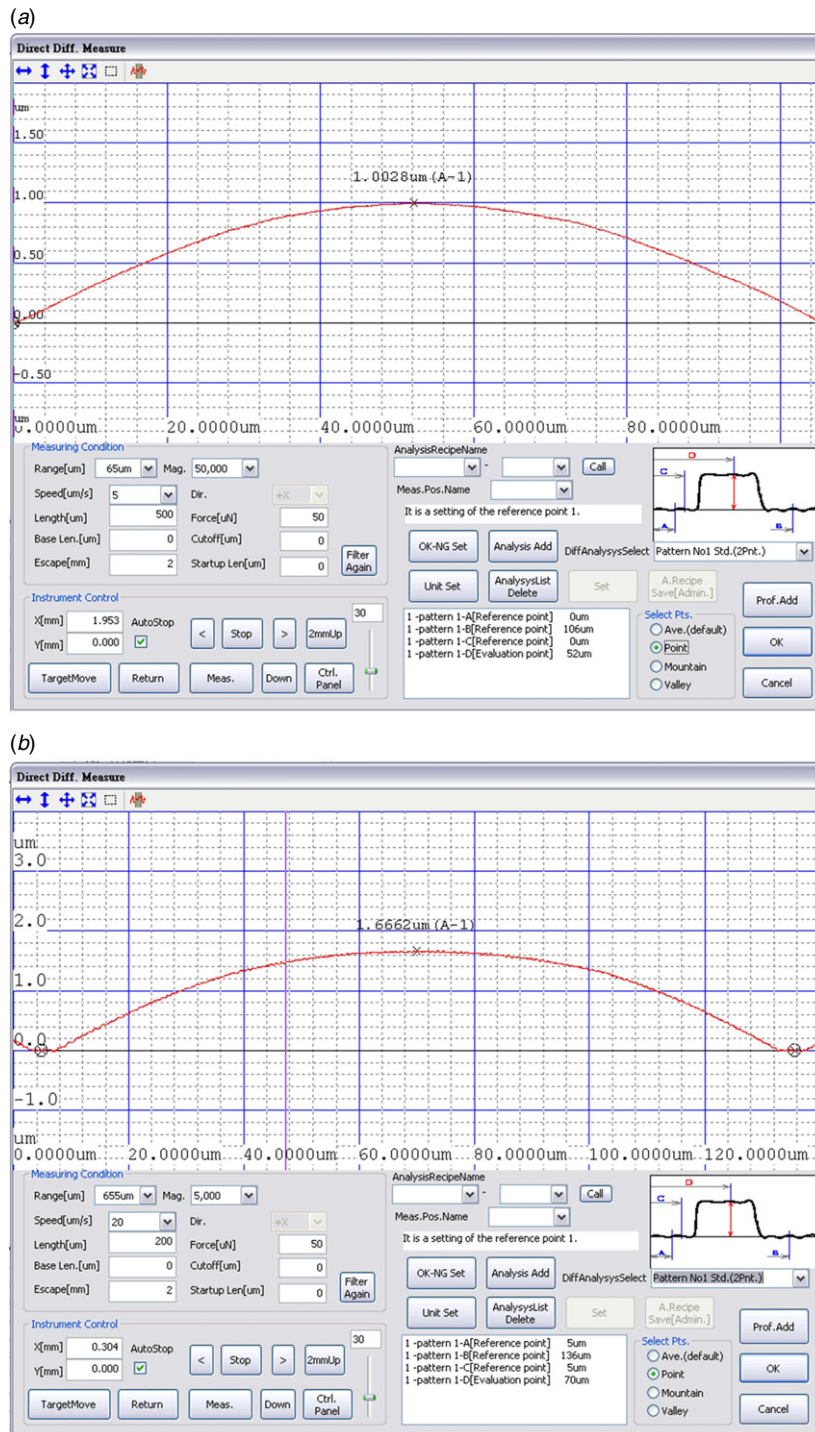
Figure 9. (*a*) Lens sag measurement results of sample#1 by Surfcorder ET3000. (*b*) Lens sag measurement results of sample#2 by Surfcorder ET3000.

4.2. Measurement results of surface profile of multi-microlenses

Two types of microlens arrays (sample#1 and sample#2) with different scales are measured by the proposed system. The microlens specification is provided by the manufacturer, where the lens sag of sample#1 is 0.97 μm, and the diameter is 110 μm; the lens sag of sample#2 is 1.63 μm, and the diameter is 126 μm. In order to validate the accuracy of the proposed method, the lens sags of sample#1 and sample#2 are

also measured by the Surfcorder ET3000, which is a contact measurement equipment that uses a contact probe to scan the 2D surface profile of the inspected object. The measurement result is shown in figure 9.

The measurement results of ten microlenses of sample#1 and sample#2 by the proposed system are expressed in the form of the arithmetic mean and the root mean square error, as summarized in table 1. The fringe pattern of sample#1 is shown in figure 4(*a*), where the 3D surface profile is rebuilt
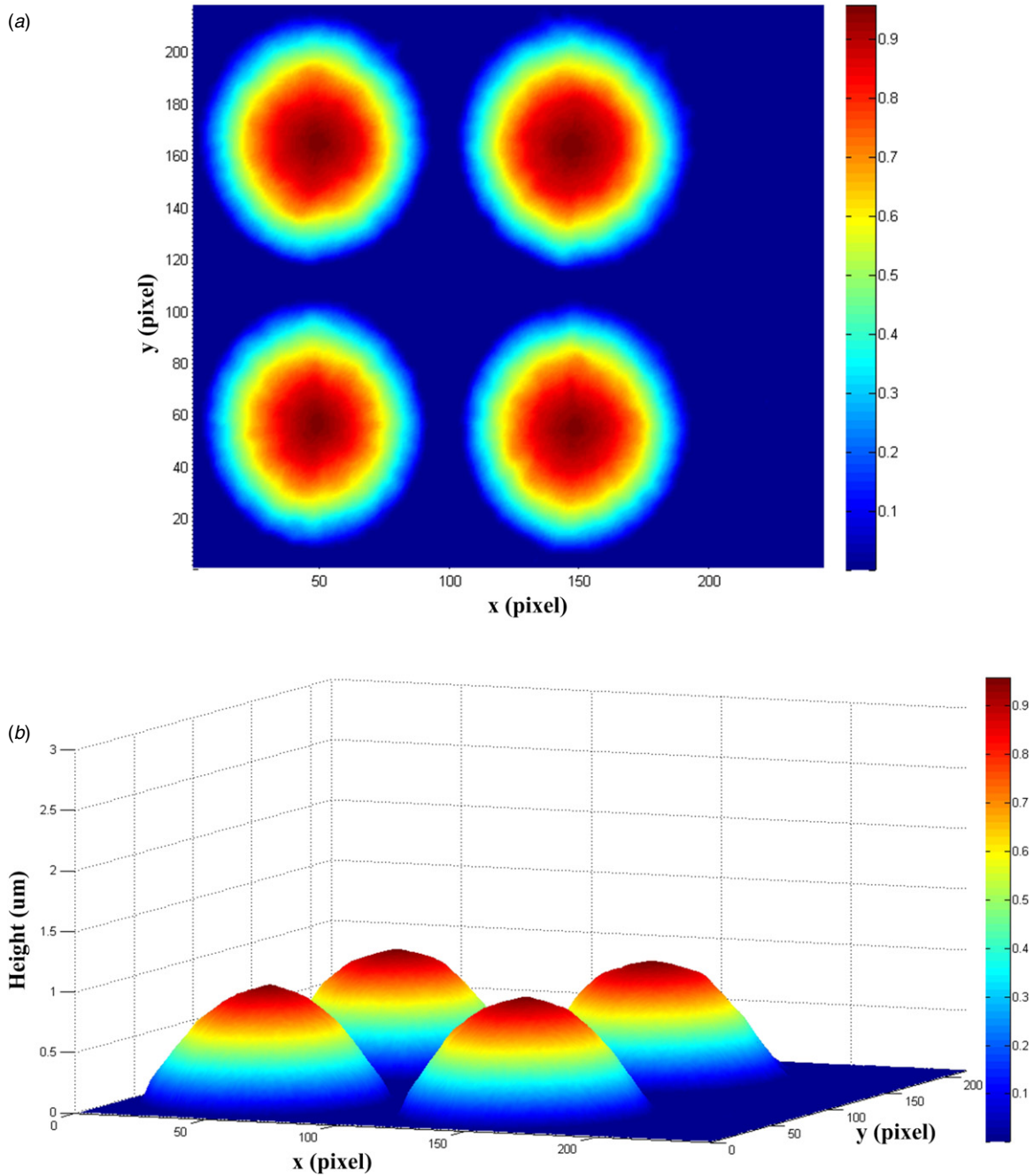
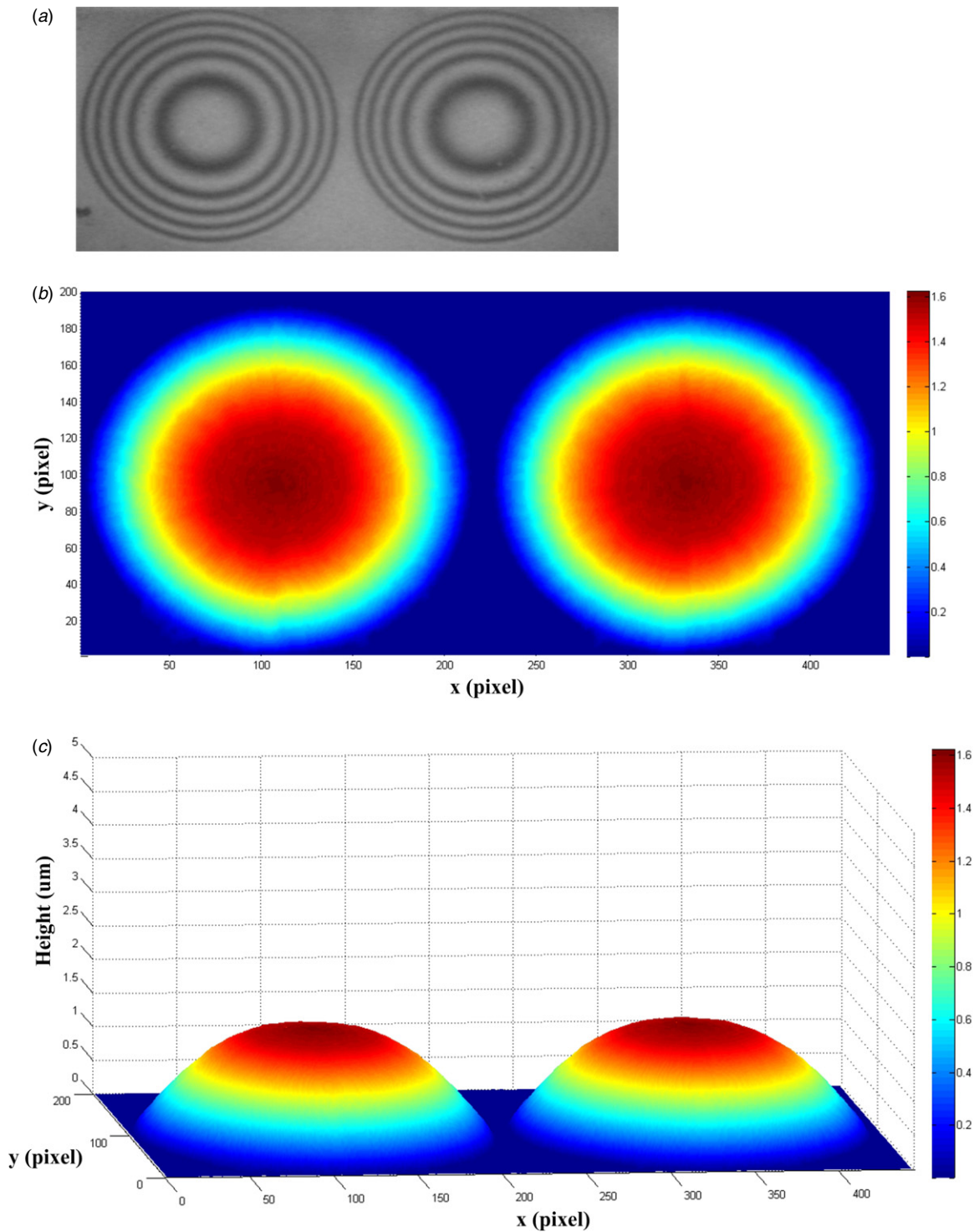**Figure 10.** 3D surface profile of sample#1 by the proposed method. (*a*) Top view. (*b*) Side view.

Table 1. Lens sag measurement results of sample#1 and sample#2 by the proposed method.

Inspected microlens	Proposed method (μm)	Referenced true value (μm)
Sample#1	0.95 ± 0.03	0.97
Sample#2	1.62 ± 0.04	1.63

by the proposed method and is smoothed by the median filter, as shown in figure 10. The fringe pattern of sample#2 and the corresponding 3D surface profile are shown in figure 11.

4.3. Experimental results of inspection path optimization

There are nearly 7500 microlenses in the used microlens array sample, and the lens spacing is 120 μm. Three different sampling inspections of microlens arrays are simulated in order to evaluate the performance of the proposed path optimization method. According to figure 1(*a*), 100, 225, and 324 microlenses are selected for sampling inspection, as based on the sampled regions of different sizes. According to the aforesaid conditions, the positioning time of the line-scan inspection path, the method of [20], and the proposed method are compared. The method in [20] simply uses the path length as the convergence condition of GA for seeking the optimal

8

(*a*)

(*b*)

(*c*)

Figure 11. 3D surface profile of sample#2 by the proposed method. (*a*) The fringe pattern. (*b*) Top view. (*c*) Side view.

inspection path, and the XY-table moves at a steady speed. Therefore, for the results obtained by redoing the method of [20], we also calculate the positioning time of the XY-table using the acceleration model as one of the compared targets.

The optimal inspection paths of 100 microlenses, as obtained by the above methods, are shown in figure 12. Note that in the experiments of sampling inspection, the starting points of obtained inspection paths are set as the top left microlens, and some subpaths that cause motor reverse are

specifically labeled by green lines. The time consumption data of three positioning experiments considering motor reverse are summarized in tables 2–4.

4.4. Discussion of measurement results

According to table 1, the lens sags of microlenses with different sizes can be correctly measured by the proposed system. In comparison to the Surfcorder ET3000 and other non-contact
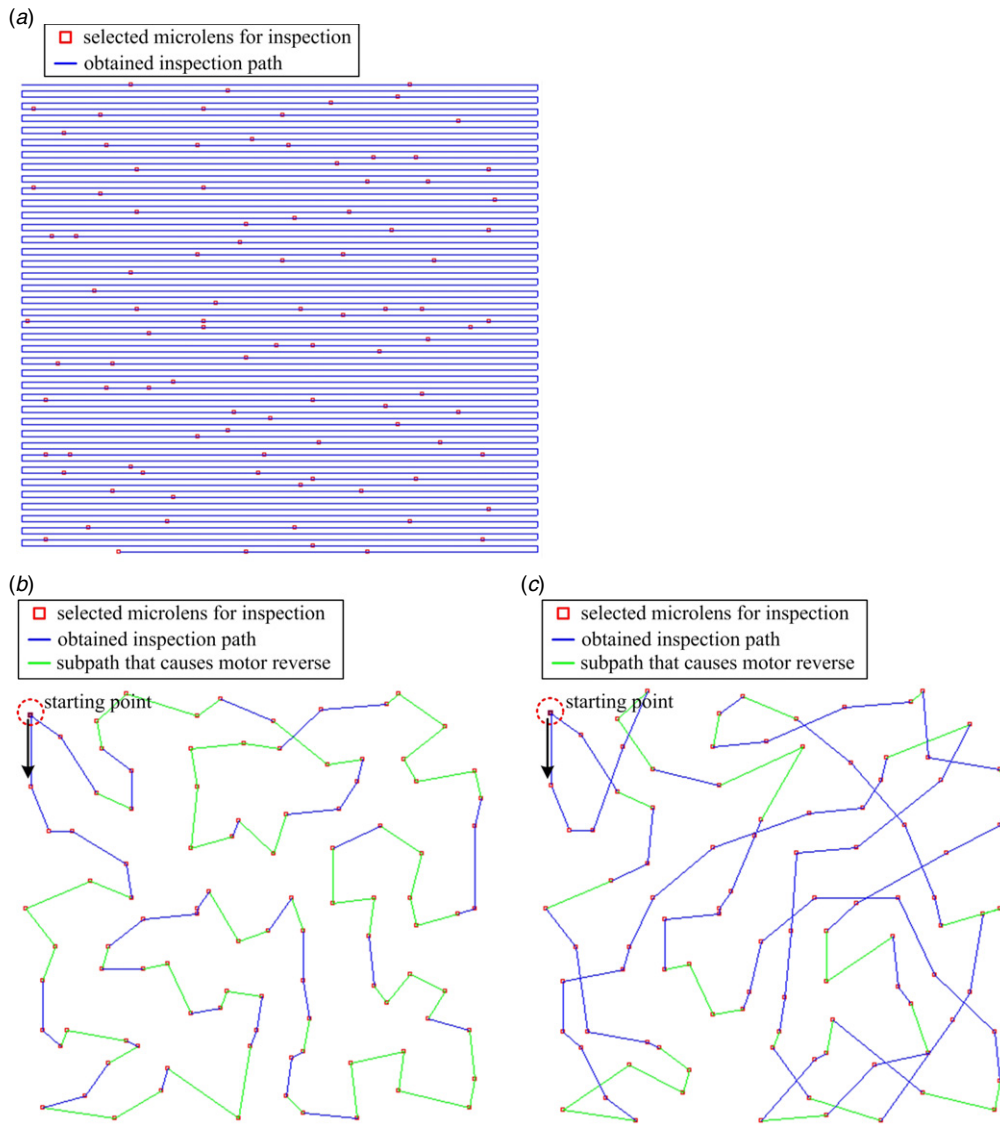
Figure 12. Inspection paths of the sampling inspection for the microlens array. (*a*) Result of the line-scan path. (*b*) Result of redoing the method in [20]. (*c*) Result of the proposed method.

Table 2. Comparisons of positioning time for 100 microlenses by the four methods.

	Total path length (mm)	No. of motor reverses	Positioning time (s)	No. of accelerated subpaths (total = 100)
Line-scan path with steady speed	802.85	154	2646.1	–
Method of [20]	88.64	58	290.1	–
Method of [20] with accelerated motion	88.64	58	238.5	29
Proposed method	115.49	30	221.4	64

Table 3. Comparisons of positioning time for 225 microlenses by the four methods.

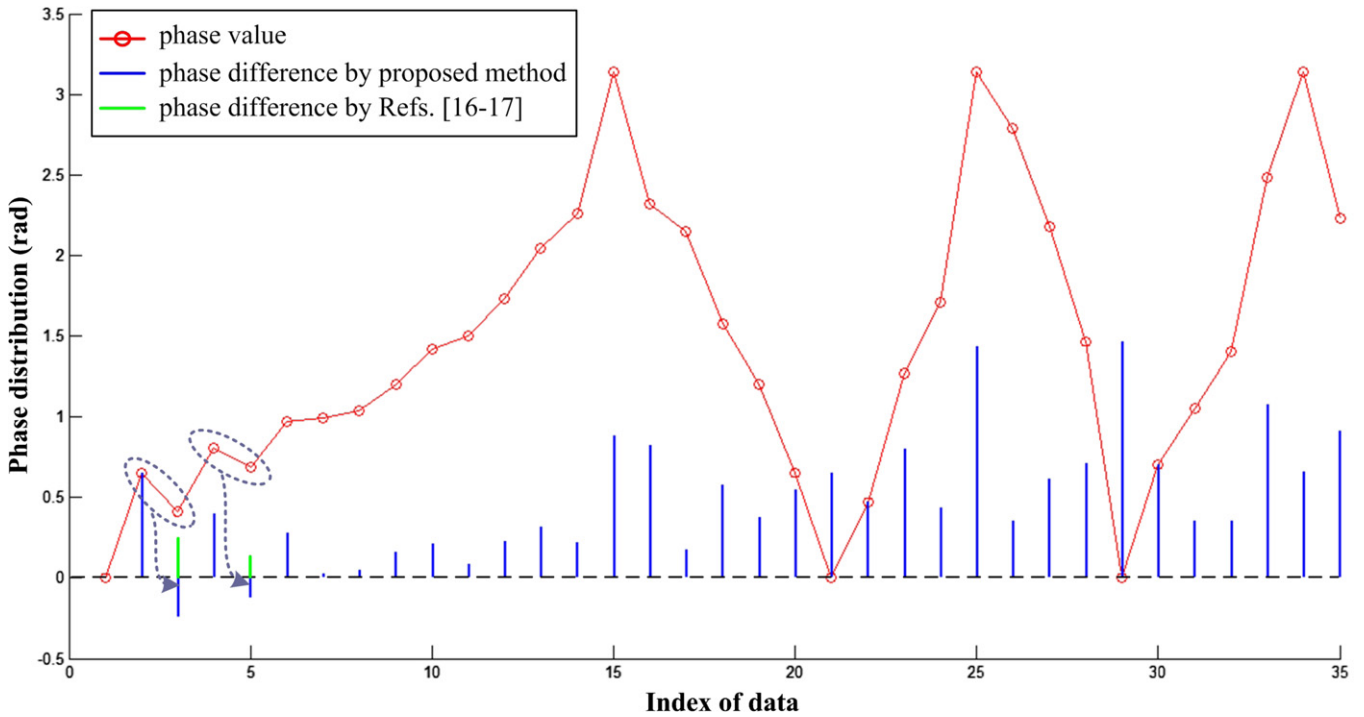|	Total path length (mm)	No. of motor reverses	Positioning time (s)	No. of accelerated subpaths (total = 225)
Line-scan path with steady speed	770.93	148	2541.0	–
Method of [20]	128.52	120	429.8	–
Method of [20] with accelerated motion	128.52	120	426.8	2
Proposed method	172.75	56	388.9	67

Figure 13. The phase difference error in [16–17] is eliminated by the proposed method.

Table 4. Comparisons of positioning time for 324 microlenses by the four methods.

	Total path length (mm)	No. of motor reverses	Positioning time (s)	No. of accelerated subpaths (total = 324)
Line-scan path with steady speed	742.61	142	2447.4	–
Method of [20]	157.27	158	534.8	–
Method of [20] with accelerated motion	157.27	158	520.1	8
Proposed method	188.13	88	477.1	51

type instruments, the proposed system is lower cost because of its simple structure, and is able to avoid scratching the lens surface and to provide the ability of rapid 3D surface profile measurement by using only a single fringe pattern. The measurement uncertainty of the proposed system can be analyzed according to equation (12). In this approach, the overall relative uncertainty [24, 25] of the microlens 3D surface profile ($\Delta H/H$) resulted from each independent source including the wavelength variation of the used laser ($\Delta\lambda/\lambda = 1.5 \times 10^{-2}$), the deviation of the phase difference ($\Delta\phi/\phi = 3.0 \times 10^{-2}$) caused by the misjudgment of real boundary pixels and the refractive index variation ($\Delta n_0/n_0 = 1.0 \times 10^{-4}$, where n_0 is the refractive index of air). Hence, the overall relative uncertainty can be obtained by:

$$\frac{\Delta H}{H} = \left(\left(\frac{\Delta\lambda}{\lambda} \right)^2 + \left(\frac{\Delta\phi}{\phi} \right)^2 + \left(\frac{\Delta n_0}{n_0} \right)^2 \right)^{1/2}. \quad (13)$$

From the above data, a relative error of 3.4% (max) can be achieved by the proposed system.

In addition, since the phase difference in equation (11) is calculated through the concept of sign reversal, the possible errors in [16, 17] when the inspected surface does not

continuously increase or decrease are eliminated, as shown in figure 13. The microlens center positioning technique is applicable to multi-microlenses or a single microlens, and the computational process of phase retrieving is also simplified, which enhances the applicability of the proposed system.

The need for high speed sampling inspection can be also fulfilled by the proposed algorithm of inspection path optimization, which is free from training parameters and is easy to be implemented. According to table 2–4, the obtained inspection path of the proposed method is most efficient among the four methods. Note that the line-scan path length is obviously dependent on the distribution of inspected microlenses, but not completely proportional to the quantity of the inspected microlenses. If the distribution of microlenses is loose in sampling inspection, the XY-table still needs to position according to various rows, and many line-scan paths without an inspected microlens will waste positioning time, thus, it is inapplicable to the sampling inspection of microlens arrays. In comparison to [20], the positioning time of the proposed method is shortened by 10 to 30% in general. The obtained optimal inspection path has less motor reverse and more accelerable subpaths. In other words,

the minimum path length does not guarantee the shortest time of XY-table positioning, while the designed fitness function considering the acceleration characteristics of the XY-table can robustly determine the optimal inspection path for the sampling inspection of microlens arrays.

5. Conclusions

This study designed an automatic optical inspection system based on a modified Fizeau interferometer as the total solution for the sampling inspection and full inspection of microlens arrays. The center of each complete microlens fringe in the image can be automatically found by the concept of clustering, and the radial lines are then built according to these microlens centers and edge points. By locating the extreme points on every radial line, the three-dimensional surface profiles of multi-microlenses can be reconstructed through a single fringe pattern. In addition, the proposed system uses the Genetic Algorithm to calculate the inspection path for the sampling inspection of the microlens array. After experimental verification, the proposed system, which considers the acceleration characteristics of the XY-table, can robustly determine the optimal inspection path, thus, greatly improving the processing speed of the microlens array measurement.

Acknowledgment

References

[1] Su D and Li X 2010 Fractionized calibration of the sample stage used in an AFM-probe mechanical testing system *Opt. Lasers Eng.* **48** 1076–81

[2] Seah M P 2013 Nanoscale roughness and bias in step height measurements by atomic force microscopy *Meas. Sci. Technol.* **24** 035004

[3] Spyratou E, Asproudis I, Tsoutsi D, Bacharis C, Moutsouris K, Makropoulou M and Serafetinides A A 2010 UV laser ablation of intraocular lenses: SEM and AFM microscopy examination of the biomaterial surface *Appl. Surf. Sci.* **256** 2539–45

[4] Müller S A, Müller D J and Engel A 2011 Assessing the structure and function of single biomolecules with scanning transmission electron and atomic force microscopes *Micron* **42** 186–95

[5] Lee D H and Cho N G 2012 Assessment of surface profile data acquired by a stylus profilometer *Meas. Sci. Technol.* **23** 105601

[6] Foreman M R, Giusca C L, Coupland J M, Török P and Leach R K 2013 Determination of the transfer function for optical surface topography measuring instruments—a review *Meas. Sci. Technol.* **24** 052001

[7] Gesualdi M R R, Soga D and Muramatsu M 2007 Surface contouring by phase-shifting real-time holography using photorefractive sillenite crystals *Opt. Laser Technol.* **39** 98–104

[8] Du H, Zhao H, Li B, Zhao J and Cao S 2012 Three frames phase-shifting shadow moiré using arbitrary unknown phase steps *Meas. Sci. Technol.* **23** 105201

[9] Zhu M, Bai F, Gan S, Huang K, Huang L and Wang J 2013 Error compensation of four and five buckets wavefront extraction algorithms in phase-shifting interferometer *Optik* **124** 5624–7

[10] Abdelsalam D G 2013 A comparison of digital holographic microscopy and on-axis phase-shifting interferometry for surface profiling *Measurement* **46** 4121–6

[11] Bruno L and Poggialini A 2013 Phase-shifting interferometry by an open-loop voltage controlled laser diode *Opt. Commun.* **290** 118–25

[12] Joo K N 2012 Fourier domain analysis on continuously scanned structured illumination microscopy *Meas. Sci. Technol.* **23** 057002

[13] Tien C L and Zeng H D 2010 Measuring residual stress of anisotropic thin film by fast Fourier transform *Opt. Express* **18** 16594–600

[14] Fernandez S, Gdeisat M A, Salvi J and Burton D 2011 Automatic window size selection in windowed Fourier transform for 3D reconstruction using adapted mother wavelets *Opt. Commun.* **284** 2797–807

[15] Fu Y, Wu J and Jiang G 2012 Fourier transform profilometry based on defocusing *Opt. Laser Technol.* **44** 727–33

[16] Lin C S, Loh G H, Fu S H, Yang S W, Chang H K and Yeh M S 2010 An automatic evaluation method for the surface profile of the microlens array using an optical interferometric microscope *Meas. Sci. Technol.* **21**

[17] Yang S W, Lin C S and Lin S K 2013 3D surface profile measurement of unsymmetrical microstructure using Fizeau interferometric microscope *Opt. Lasers Eng.* **51** 348–57

[18] Yang X, Yu Q and Fu S 2009 Determination of skeleton and sign map for phase obtaining from a single ESPI image *Opt. Commun.* **282** 2301–6

[19] Lin C S, Lin C H, Lin C C and Yeh M S 2010 Three-dimensional profile measurement of small lens using subpixel localization with color grating *Optik* **121** 2122–7

[20] Yang S W, Lin C S, Lin S K, Fu S H and Yeh M S 2013 An automatic optical inspection system for measuring a microlens array with an optical interferometric microscope and genetic algorithm *Assem. Autom.* **33** 57–67

[21] He Y and Hui C W 2008 A rule-based Genetic Algorithm for the scheduling of single-stage multi-product batch plants with parallel units *Comput. Chem. Eng.* **32** 3067–83

[22] Baker B M and Ayechew M A 2003 A genetic algorithm for the vehicle routing problem *Comput. Oper. Res.* **30** 787–800

[23] Lin C S, Wu K C, Lay Y L, Lin C C and Lin J M 2009 An automatic template generating method of machine vision system in TFT LCD assembly and positioning process with genetic algorithm *Assem. Autom.* **29** 41–48

[24] ISO 1993 *Guide to the Expression of Uncertainty in Measurement* (Geneva: International Organization for Standardization)

[25] Tien C L and Zeng H D 2010 Measuring residual stress of anisotropic thin film by fast Fourier transform *Opt. Express* **18** 16594–600